

Cite this: *Energy Environ. Sci.*,
2019, 12, 2581

High light-to-fuel efficiency and CO₂ reduction rates achieved on a unique nanocomposite of Co/Co doped Al₂O₃ nanosheets with UV-vis-IR irradiation†

Shaowen Wu, Yuanzhi Li, * Qian Zhang, Zhongkai Jiang, Yi Yang, Jichun Wu and Xiujian Zhao 

A unique nanocomposite of Co nanoparticles supported on Co doped Al₂O₃ nanosheets (Co/Co–Al₂O₃) was synthesized by a facile method. For photothermocatalytic CO₂ reduction with CH₄ under focused UV-visible-infrared (UV-vis-IR) irradiation, Co/Co–Al₂O₃ exhibits high light-to-fuel efficiency (27.1%) and production rates of CO and H₂ (43.46 and 39.42 mmol min⁻¹ g⁻¹). Even with λ > 690 nm focused vis-IR irradiation, it still exhibits high light-to-fuel efficiency (23.2%) and production rates of CO and H₂ (24.62 and 18.97 mmol min⁻¹ g⁻¹). It is found that supporting Co nanoparticles on Co doped Al₂O₃ nanosheets significantly improves the photothermocatalytic durability compared to a reference catalyst of Co nanoparticles on Al₂O₃ nanosheets (Co/Al₂O₃). The improved durability is attributed to the fact that O atoms from Co doped Al₂O₃ in Co/Co–Al₂O₃ participate in the oxidation of C* species formed by both the complete dissociation of CH₄ and the disproportionation of the produced CO as side-reactions of carbon deposition, thus significantly reducing the carbon deposition rate. The high photothermocatalytic activity is attributed to effective light-driven thermocatalysis, substantially boosted by new photoactivation: Co nanoparticles in Co/Co–Al₂O₃ act as thermocatalytic components. Both Co nanoparticles and Co doped Al₂O₃ in Co/Co–Al₂O₃ act as light absorbers due to their strong absorption over the entire solar spectral region. Their efficient photothermal conversion together with the IR heating effect of the focused irradiation causes an elevation in the surface temperature of Co/Co–Al₂O₃, thus triggering the thermocatalytic reaction. The focused irradiation substantially reduces the activation energy for CO₂ reduction by CH₄ on Co/Co–Al₂O₃, thus considerably promoting the catalytic activity. The photoactivation also promotes catalyst durability due to the inhibition of carbon deposition by CO disproportionation.

Received 8th May 2019,
Accepted 27th June 2019

DOI: 10.1039/c9ee01484e

rsc.li/ees

Broader context

Energy shortages and severe environmental issues induced by enormous CO₂ discharges are primary global challenges. Photocatalytic CO₂ reduction is especially attractive, as it can not only actualize solar energy storage, but also tackle global warming induced by CO₂. However, low solar-to-fuel efficiencies and low CO₂ reduction rates are primary obstacles for actualizing the targets. Photocatalysis for solar fuels is based on the efficient separation of photogenerated charge carriers on diverse semiconductors. But the majority of the solar energy absorbed by semiconductors is lost in the form of thermal energy through the fast combination of charge carriers. The key to overcoming these obstacles is to search for new photocatalysts and/or new strategies different from photocatalysis that can utilize the lost thermal energy. In this work, we achieve high light-to-fuel efficiency (27.1%) and production rates of CO and H₂ (43.46 and 39.42 mmol min⁻¹ g⁻¹) through photothermocatalytic CO₂ reduction by CH₄ (the main component of abundant natural gas resources) on a unique nanocomposite of Co nanoparticles supported on Co doped Al₂O₃ nanosheets with UV-vis-IR irradiation. This work provides an outstanding approach for tackling the issues of solar energy storage and global warming induced by CO₂.

State Key Laboratory of Silicate Materials for Architectures
(Wuhan University of Technology), 122 Luoshi Road, Wuhan 430070, P. R. China.
E-mail: liyuanzhi66@hotmail.com

† Electronic supplementary information (ESI) available. See DOI: 10.1039/c9ee01484e

1. Introduction

Energy shortage and the severe environmental issue induced by the enormous discharge of CO₂ as a greenhouse gas due to the

combustion of fossil fuels are primary challenges in the world. Solar energy is an inexhaustible renewable energy in which UV, visible, and infrared energy account for about 5%, 45%, and 50%, respectively. The efficient conversion and storage of solar energy are important approaches to addressing the energy shortage. Photovoltaics is an efficient approach to convert solar energy to electricity, which has achieved huge commercial applications. Due to the intermittent characteristics of solar light day and night, solar energy storage is urgently needed. Photocatalysis for solar fuels, such as photocatalytic overall water splitting^{1–12} and CO₂ reduction to produce fuels,^{1,13–35} provides a promising approach for solar energy storage, and is thus attracting extensive interest. Among these techniques, photocatalytic CO₂ reduction^{13–26} is especially attractive as it could not only actualize solar energy storage, but also tackle the global warming induced by CO₂. Both photovoltaics and photocatalysis are based on the efficient separation of photogenerated charge carriers on diverse semiconductors upon solar light absorption. Although a variety of approaches have been developed to improve the separation efficiency of charge carriers, the majority of the solar energy absorbed by semiconductors is lost in the form of thermal energy *via* the fast recombination of photogenerated charge carriers.^{2,36,37} Searching for a strategy of efficiently utilizing the lost thermal energy is crucial for considerably improving solar-to-electricity efficiency and solar-to-fuel efficiency. In principle, it is impossible to get high solar-to-fuel efficiency in photocatalysis comparable to solar-to-electricity efficiency in a solar cell because it not only depends on the separation efficiency of the charge carriers in the semiconductor, but also on the efficiency of the transfer of charge carriers from the semiconductor to the reactant molecules. Reducing the band gap of semiconductors is a very important approach to improving solar-to-fuel efficiency, as it is able to extend the absorption region of solar light to visible or even to near-infrared light. However, the band gap reduction causes a decrease in the reduction ability of photogenerated electrons in the conduction band and/or the oxidation ability of photogenerated holes in the valence band. Eventually, photogenerated electrons and holes electrochemically lose the ability to trigger the reaction of photocatalytic fuel production.^{38,39} The requirement of band gap matching makes it extremely difficult to utilize infrared energy from solar light for photocatalytic fuel production. Actually, up to now, there have been no reports on infrared light-to-fuel conversion by photocatalysis without using a sacrificial reagent. Currently, the insurmountable obstacle for solar fuels is the low solar-to-fuel efficiency, far below the goal of 10% for practical applications.^{1,2,40} Another obstacle is the low production rate of solar fuels, especially through photocatalytic CO₂ reduction. Extensive work has been devoted to leaping over these obstacles.^{1–35} Up to now, the maximum record for solar-to-fuel efficiency for photocatalytic fuel production is 2%.⁴ The maximum records of CO₂ reduction rate for photocatalytic CO₂ reduction using an organic sacrificial reagent²⁹ and without using a sacrificial reagent¹³ are 2.62×10^4 and $488.4 \mu\text{mol h}^{-1} \text{g}^{-1}$ (0.44 and $0.00814 \text{ mmol min}^{-1} \text{g}^{-1}$), respectively. It is highly desirable to design new photocatalysts and/or to develop a new strategy

different from photocatalysis to significantly boost solar-to-fuel efficiency and the solar fuel production rate.

Recently, a strategy of light-assisted reduction of CO₂ with CH₄ (the main component of the abundant natural gas resource) to produce fuels of H₂ and CO (CO₂ + CH₄ = 2CO + 2H₂, $\Delta H_{298} = 247 \text{ kJ mol}^{-1}$) has been developed by several research groups.^{41–43} It was reported that the CO₂ reduction rate was considerably boosted by light irradiation using several catalysts, such as Pt/TiO₂,⁴¹ Rh-Au/SBA-15, Ni/Al₂O₃, Fe/SiO₂, and Rh/SiO₂.^{42,43} The strategy is very attractive because the strong endothermic property of the reaction ($\Delta H_{298} = 247 \text{ kJ mol}^{-1}$), like photocatalytic overall water splitting (2H₂O(l) = 2H₂ + O₂, $\Delta H_{298} = 285.8 \text{ kJ mol}^{-1}$)⁴ and photocatalytic CO₂ reduction^{13,14} (e.g. CO₂ = CO + 0.5O₂, $\Delta H_{298} = 283.0 \text{ kJ mol}^{-1}$), makes it possible to actualize efficient solar-to-fuel energy storage. Moreover, the products of CO and H₂ are not only fuels, but also the feedstocks for synthesizing important chemicals and liquid fuels from natural gas,⁴¹ which is an important target in the petrochemical industry. As an additional electric heater was used in the light-assisted reduction of CO₂ with CH₄, the light-to-fuel efficiency was not reported.^{41–43} In addition, the reported catalysts experienced obvious deactivation within several hours.^{41–43} The fast deactivation of the catalyst is mainly ascribed to thermodynamically inevitable carbon deposition side-reactions, such as the complete dissociation of CH₄ (CH₄ = C + 2H₂, $\Delta H_{298} = 75 \text{ kJ mol}^{-1}$) and the disproportionation of the produced CO (2CO = C + CO₂, $\Delta H_{298} = -171 \text{ kJ mol}^{-1}$) at a high reaction temperature.^{44,45} Addressing the catalyst deactivation problem is greatly challenging and extremely difficult. Very recently, we actualized the highly effective photothermocatalytic reduction of CO₂ with CH₄ without using any additional heater besides a light source.^{45–47} A high CO₂ reaction rate and light-to-fuel efficiency (up to 12.5%) were simultaneously achieved by designing several nanostructured photothermocatalysts with good durability, such as silica cluster modified Ni nanoparticles and Pt nanoparticles embedded in mesoporous CeO₂. Rationally designing an excellent photothermocatalyst for the photothermocatalytic strategy is crucial for further significantly boosting the CO₂ reaction rate and light-to-fuel efficiency, and improving catalyst durability by kinetically inhibiting carbon deposition.

Herein, we have designed a unique nanocomposite of Co nanoparticles supported on Co doped Al₂O₃ nanosheets (Co/Co–Al₂O₃). For photothermocatalytic CO₂ reduction by CH₄ under focused UV-vis-IR irradiation, Co/Co–Al₂O₃ demonstrates a high light-to-fuel efficiency (27.1%) and production rates of CO and H₂ (43.46 and $39.42 \text{ mmol min}^{-1} \text{g}^{-1}$). It is found that supporting Co nanoparticles on Co doped Al₂O₃ significantly improves the catalyst durability in comparison with a reference catalyst of Co nanoparticles supported on Al₂O₃ nanosheets (Co/Al₂O₃). The high photothermocatalytic activity of Co/Co–Al₂O₃ is ascribed to effective light-driven thermocatalysis that is substantially boosted by a new photoactivation. The new photoactivation also promotes the catalyst durability. On the basis of the experimental evidence, we unveil the origin of the excellent photothermocatalytic performance of Co/Co–Al₂O₃ and the novel photoactivation.

2. Results and discussion

2.1. Characterization

The unique nanocomposite of Co nanoparticles supported on Co doped Al_2O_3 nanosheets (labeled Co/Co- Al_2O_3) was prepared by a hydrothermal reaction among $\text{Co}(\text{NO}_3)_2$, $\text{Al}(\text{NO}_3)_3$, and $\text{CO}(\text{NH}_2)_2$ with a Co/(Co + Al) molar ratio of 0.09 at 150 °C, subsequently calcined at 500 °C, and finally pre-reduced at 700 °C in a flow of 5 vol% H_2/Ar (see Experimental, ESI†). By the same procedure, except for decreasing the Co/(Co + Al) molar ratio to 0.05, Co doped Al_2O_3 nanosheets (labeled Co- Al_2O_3) were prepared. By the same procedure, except for no addition of $\text{Co}(\text{NO}_3)_2$, pure Al_2O_3 was obtained. For comparison, a nanocomposite of Co nanoparticles supported on Al_2O_3 nanosheets (labeled Co/ Al_2O_3) was prepared (see Experimental). ICP-OES analysis demonstrates that the Co/Al molar ratios of Co- Al_2O_3 , Co/Co- Al_2O_3 , and Co/ Al_2O_3 are 0.0386, 0.0751, and 0.0867, respectively. XRD analysis demonstrates that pure Al_2O_3 has a cubic crystalline structure of $\gamma\text{-Al}_2\text{O}_3$ (PDF 10-0425) (Fig. 1). Co- Al_2O_3 has the same XRD patterns as pure Al_2O_3 , and no XRD peaks of any cobalt oxide or metallic cobalt are observed. The observation indicates that Co doping does not alter the cubic crystalline structure of $\gamma\text{-Al}_2\text{O}_3$, and the pre-treatment at 700 °C in a flow of 5 vol% H_2/Ar does not lead to the reduction of Co- Al_2O_3 to metallic cobalt. For Co/Co- Al_2O_3 , XRD peaks of metallic cobalt (PDF 15-0806), besides the XRD peaks of $\gamma\text{-Al}_2\text{O}_3$, are observed. The result indicates that increasing the Co/(Co + Al) molar ratio from 0.05 (Co- Al_2O_3) to 0.09 leads to the formation of metallic cobalt besides Co doped Al_2O_3 . The average crystal size of metallic cobalt, estimated in accordance with the Scherrer formula ($L = 0.89\lambda/\beta \cos \theta$) at the peak of the {111} facet ($2\theta = 44.22^\circ$), is 19.5 nm. Co/ Al_2O_3 has XRD patterns similar to those of Co/Co- Al_2O_3 . Metallic cobalt and $\gamma\text{-Al}_2\text{O}_3$ are observed. The average crystal size of metallic cobalt in Co/ Al_2O_3 is 24.1 nm.

The SEM image shows that Co/Co- Al_2O_3 has the morphology of nanosheets of hundreds of nanometers in length and dozens of nanometers in thickness (Fig. 2A). TEM images show that metallic Co nanoparticles (black dots) with sizes of 8–28 nm are distributed on Co- Al_2O_3 nanosheets (Fig. 2B and C). The predominant size of the Co nanoparticles is 14–18 nm

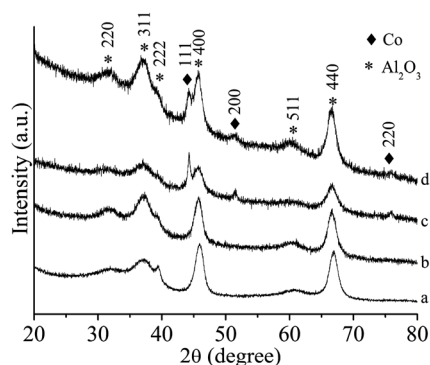


Fig. 1 XRD patterns of Al_2O_3 (a), Co- Al_2O_3 (b), Co/ Al_2O_3 (c), and Co/Co- Al_2O_3 (d).

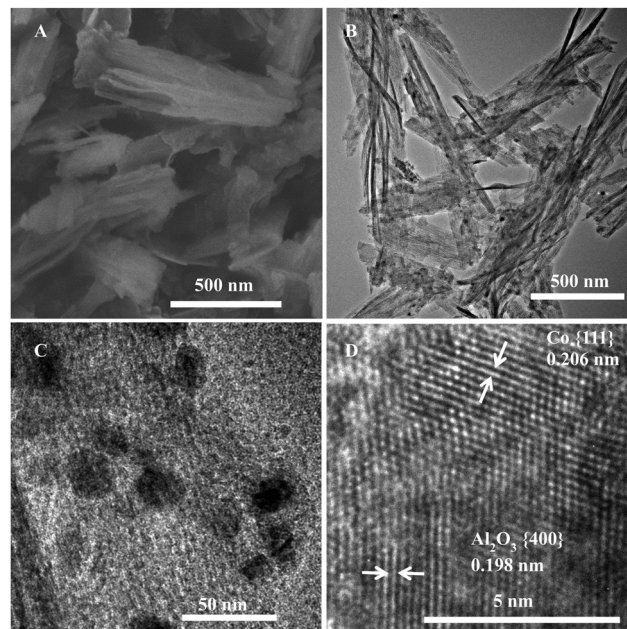


Fig. 2 An SEM image (A), TEM images (B and C), and a HRTEM image (D) of Co/Co- Al_2O_3 .

(Fig. S1, ESI†), which is generally in agreement with the result by XRD. The HRTEM image shows that a metallic cobalt nanocrystal with a lattice spacing of {111} facets is in close contact with $\gamma\text{-Al}_2\text{O}_3$ with a lattice spacing of {400} facets (Fig. 2D). As can be seen from the HAADF image (Fig. 3A) and the corresponding Co elemental mapping (Fig. 3B), segregated Co nanoparticles are observed, which is in agreement with the result by XRD. Moreover, besides Co nanoparticles, Co is also uniformly distributed on Co/Co- Al_2O_3 (Fig. 3B). The elemental mappings of Al and O demonstrate that Al and O are uniformly distributed on Co/Co- Al_2O_3 (Fig. 3C and D). Co/Co- Al_2O_3 is further characterized by high-resolution HAADF-STEM. Metallic Co nanocrystals with a lattice spacing of 0.206 nm (bright lines) and randomly distributed Co (bright dots) are observed (Fig. 3E and F). The observations together with the results of ICP and XRD clearly demonstrate that Co/Co- Al_2O_3 has a unique microstructure of Co nanoparticles supported on Co doped Al_2O_3 nanosheets rather than Co nanocrystals supported on Al_2O_3 nanosheets.

For Co- Al_2O_3 , the SEM image (Fig. S2A, ESI†) shows that Co- Al_2O_3 has the morphology of nanosheets. TEM images confirm the nanosheet morphology of Co- Al_2O_3 (Fig. S2B and C, ESI†). The HRTEM image shows a lattice spacing of {400} facets of $\gamma\text{-Al}_2\text{O}_3$ (Fig. S2D, ESI†). No lattice spacings of metallic cobalt or cobalt oxides are observed. The HAADF image and the corresponding elemental mappings demonstrate that Co, Al, and O (Fig. S3, ESI†) are all uniformly distributed, and no segregated Co nanoparticles like Co/Co- Al_2O_3 are observed. High-resolution HAADF-STEM shows that there are randomly distributed Co (bright dots) without metallic Co nanocrystals observed for Co- Al_2O_3 (Fig. S4, ESI†). The observations together with the results of ICP and XRD clearly demonstrate that

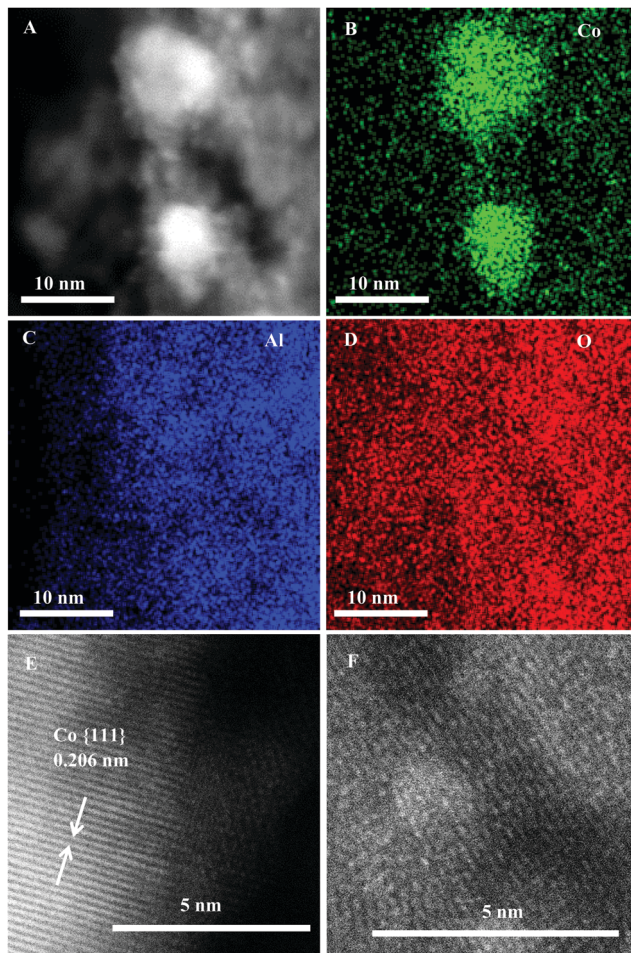


Fig. 3 A HAADF image (A) and the corresponding elemental mapping of Co (B), Al (C), and O (D) of Co/Co-Al₂O₃. A high-resolution HAADF-STEM image of Co/Co-Al₂O₃ (E and F).

Co-Al₂O₃ has a microstructure of Co uniformly doped Al₂O₃ nanosheets.

For Co/Al₂O₃, the SEM image (Fig. S5A, ESI[†]) shows that Co/Al₂O₃ has the morphology of nanosheets. TEM images show that metallic nanoparticles (black dots) with sizes of 10–40 nm are distributed on Al₂O₃ nanosheets (Fig. S5B and C). The predominant size of the Co nanoparticles is 20–22 nm (Fig. S6, ESI[†]), which is generally in agreement with the result by XRD. The HRTEM image shows that a metallic cobalt nanocrystal with a lattice spacing of {111} facets is in close contact with cubic Al₂O₃ with a lattice spacing of {400} facets (Fig. S5D, ESI[†]). As shown in the HAADF image and the corresponding elemental mappings (Fig. S7, ESI[†]), Al and O are uniformly distributed, but Co is distributed as segregated nanoparticles. This is in striking contrast to the uniform distributions of Co, Al and O for both Co/Co-Al₂O₃ and Co-Al₂O₃. The observations together with the results of ICP and XRD clearly demonstrate that Co/Al₂O₃ has a microstructure of Co nanoparticles supported on Al₂O₃ nanosheets.

The valence states of the elements in the samples were characterized by XPS (Fig. S8, ESI[†]). Al and O in Co-Al₂O₃, Co/Co-Al₂O₃ and Co/Al₂O₃ exist as Al³⁺ and O²⁻, respectively. For Co-Al₂O₃, only Co²⁺ is observed. For Co/Co-Al₂O₃ and

Co/Al₂O₃, most of Co species exist as Co²⁺. Only a small amount of Co species exists in metallic Co, which is attributed to the surface oxidation of Co nanoparticles due to exposure to air.

The samples were characterized by N₂ adsorption (Fig. S9–S11, ESI[†]). The BET surface areas of Co-Al₂O₃, Co/Co-Al₂O₃, and Co/Al₂O₃ are 199.7, 189.8, and 228.6 m² g⁻¹, respectively. The BJH adsorption pore volumes of Co-Al₂O₃, Co/Co-Al₂O₃, and Co/Al₂O₃ are 0.56, 0.49, and 0.53 cm³ g⁻¹, respectively.

2.2. Photothermocatalytic activity

The photothermocatalytic CO₂ reduction by CH₄ on the samples with focused irradiation from a 500 W Xe lamp (note: no any additional heater was used) was conducted in a home-made stainless steel reactor with a quartz window (Experimental, Scheme 1, ESI[†]).⁴⁶ A feed stream of 30.0/29.3/40.7 vol% CH₄/CO₂/Ar constantly flowed at 89.2 mL min⁻¹ into the reactor which contained 0.0200 g of the sample. As can be seen from Fig. 4, pure Al₂O₃ has no photothermocatalytic activity. Co doping enables Al₂O₃ to have photothermocatalytic activity. With the focused UV-Vis-IR irradiation, the reaction rates of CH₄ (r_{CH_4}) and CO₂ (r_{CO_2}) of Co-Al₂O₃ are 0.32 and 0.51 mmol min⁻¹ g⁻¹, respectively (Fig. 4A). The production rates of H₂ (r_{H_2}) and CO (r_{CO}) of Co-Al₂O₃ are 0.27 and 0.83 mmol min⁻¹ g⁻¹, respectively (Fig. 4B). Remarkably, supporting Co nanoparticles on Co doped Al₂O₃ nanosheets promotes the photothermocatalytic activity tremendously. Co/Co-Al₂O₃ has high photothermocatalytic activity with r_{CH_4} and r_{CO_2} values of 20.12 and 22.97 mmol min⁻¹ g⁻¹, respectively. The r_{H_2} and r_{CO} values of Co/Co-Al₂O₃ are as high as 39.42 and 43.46 mmol min⁻¹ g⁻¹, respectively. This result suggests that Co nanoparticles in Co/Co-Al₂O₃ as catalytic active sites play a crucial role in the photothermocatalytic CO₂ reduction by CH₄. The $r_{\text{H}_2}/r_{\text{CO}}$ molar ratio being less than the stoichiometric ratio (1:1) of the reaction (CO₂ + CH₄ = 2CO + 2H₂) is attributed to the occurrence of a reverse water-gas shift (H₂ + CO₂ = H₂O + CO) as a side reaction. This is verified by the detection of a small amount of moisture in the effluents with gas chromatography (GC). There are no other products besides H₂, CO, and H₂O detected by GC.

In order to make a comparison, we measured the photothermocatalytic activity of the nanocomposite of Co nanoparticles supported on Al₂O₃ nanosheets (Co/Al₂O₃). Compared to Co/Co-Al₂O₃, Co/Al₂O₃ exhibits lower photothermocatalytic activity. The r_{CH_4} and r_{CO_2} of Co/Al₂O₃ are 17.87 and 20.46 mmol min⁻¹ g⁻¹, respectively. The r_{H_2} and r_{CO} of Co/Al₂O₃ are 31.42 and 37.97 mmol min⁻¹ g⁻¹, respectively.

Due to the strong endothermic property of CO₂ reduction by CH₄ to CO and H₂ ($\Delta H_{298} = 247$ kJ mol⁻¹), the high photothermocatalytic activity of Co/Co-Al₂O₃ with focused UV-vis-IR irradiation suggests the realization of highly efficient light-to-fuel conversion. Therefore, the light-to-fuel efficiency (η) is calculated according to the following equation (ESI[†]).^{46,48}

$$\eta = \left(r_{\text{CO}} \times \Delta_c H_{\text{CO}}^0 + r_{\text{H}_2} \times \Delta_c H_{\text{H}_2}^0 - r_{\text{CH}_4} \times \Delta_c H_{\text{CH}_4}^0 \right) / P_{\text{irradiation}}$$

$\Delta_c H_{\text{CH}_4}^0$, $\Delta_c H_{\text{CO}}^0$, and $\Delta_c H_{\text{H}_2}^0$ are the standard combustion heats (298.15 K) of CH₄, CO, and H₂ as fuels, respectively (Note: $\Delta_c H_{\text{CO}_2}^0$ is 0). $P_{\text{irradiation}}$ is the irradiation power.

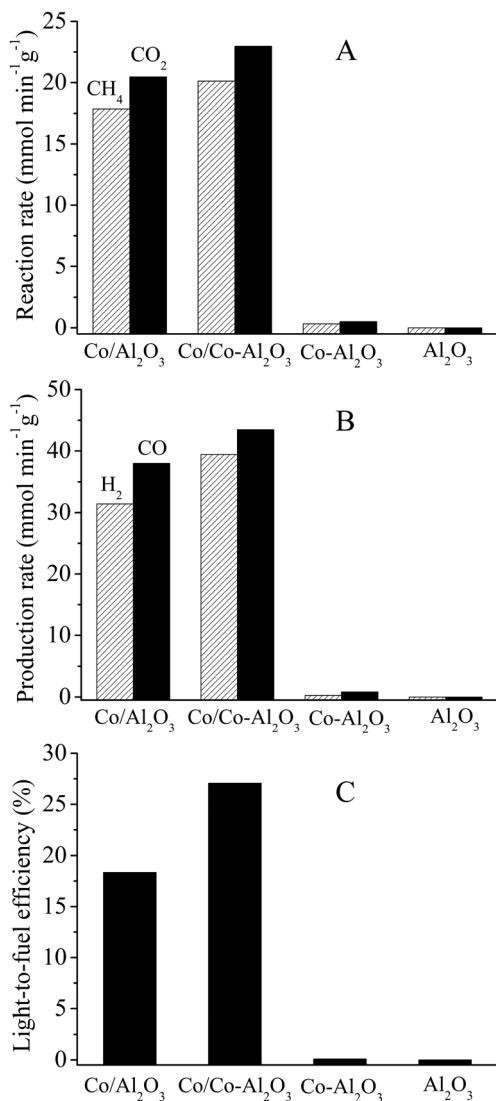


Fig. 4 Reaction rates (A), production rates (B), and light-to-fuel efficiency (C) of Al₂O₃, Co-Al₂O₃, Co/Co-Al₂O₃, and Co/Al₂O₃ for CO₂ reduction by CH₄ with focused UV-vis-IR irradiation. Note: the photothermocatalytic data from Co/Al₂O₃ in Fig. 4 are the average data in the initial 20 min as Co/Al₂O₃ experienced swift deactivation (see Fig. 6A).

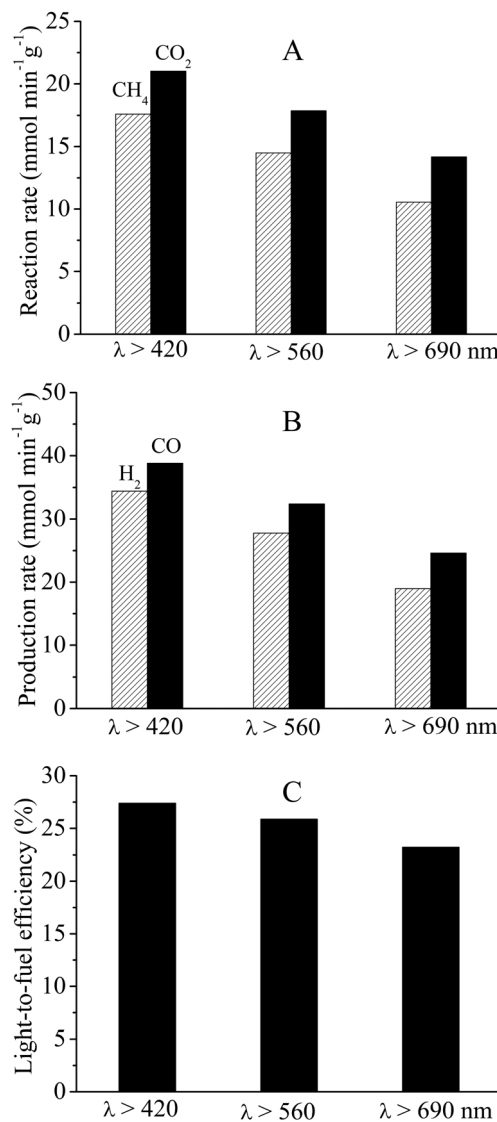


Fig. 5 Reaction rates (A), production rates (B), and light-to-fuel efficiency (C) of Co/Co-Al₂O₃ for CO₂ reduction by CH₄ with focused vis-IR irradiation.

Under focused UV-vis-IR irradiation, Co/Co-Al₂O₃ has a high η value of 27.1% (Fig. 4C). Compared to Co/Co-Al₂O₃, Co/Al₂O₃ has a much lower η value of 18.4%, while Co-Al₂O₃ has a very low η value of 0.9%.

In spite of the high light-fuel efficiency, the η value of Co/Co-Al₂O₃ is still far lower than the thermodynamic maximum value (η_{\max}) of the reaction system (59.8%, ESI[†]), which is decided by the solar absorption and Carnot efficiencies, in accordance with the following equation:^{46,48}

$$\eta_{\max} = [1 - \sigma \times T_{\text{H}}^4 / (I_{\text{DNI}} \times C)] \times [1 - T_{\text{I}} / T_{\text{H}}]$$

The photothermocatalytic CO₂ reduction by CH₄ on Co/Co-Al₂O₃ with focused vis-IR irradiation was also conducted. Co/Co-Al₂O₃ has high photothermocatalytic activity with focused vis-IR irradiation (Fig. 5). With λ > 420 nm focused vis-IR

irradiation, the r_{H_2} and r_{CO} values of Co/Co-Al₂O₃ are 34.42 and 38.80 mmol min⁻¹ g⁻¹, respectively. The η value of Co/Co-Al₂O₃ is 27.4%. Even with λ > 690 nm focused vis-IR irradiation, Co/Co-Al₂O₃ still shows high r_{H_2} and r_{CO} values of 18.97 and 24.62 mmol min⁻¹ g⁻¹. The η value of Co/Co-Al₂O₃ is still as high as 23.2%.

2.3. Photothermocatalytic durability

Good catalytic durability is very important for CO₂ reduction with CH₄, as the catalyst experiences fast deactivation due to thermodynamically inevitable carbon deposition.^{44,45} To prove whether Co/Co-Al₂O₃ and Co/Al₂O₃ are photothermocatalytically stable, long-term photothermocatalytic CO₂ reduction by CH₄ on Co/Co-Al₂O₃ and Co/Al₂O₃ with focused UV-vis-IR irradiation was conducted. As shown in Fig. 6A, although Co/Al₂O₃ has good initial photothermocatalytic activity, it is quickly deactivated.

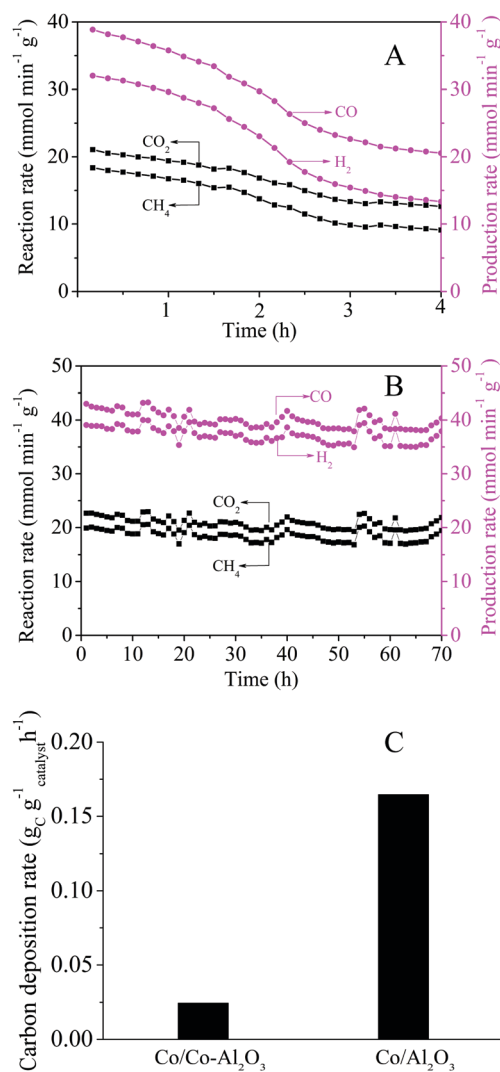


Fig. 6 Long-term time course of the reaction and production rates for CO_2 reduction with CH_4 on $\text{Co}/\text{Al}_2\text{O}_3$ (A) and $\text{Co}/\text{Co}-\text{Al}_2\text{O}_3$ (B) under focused UV-vis-IR irradiation. The carbon deposition rates of $\text{Co}/\text{Co}-\text{Al}_2\text{O}_3$ and $\text{Co}/\text{Al}_2\text{O}_3$ (C).

After 4 h of reaction, its r_{CO} and r_{H_2} values quickly reduce by 58.4% and 47.1%, respectively. The η value of $\text{Co}/\text{Al}_2\text{O}_3$ swiftly decreases from 18.4% (initial 20 min) to 7.3%. In striking contrast, $\text{Co}/\text{Co}-\text{Al}_2\text{O}_3$ exhibits excellent photothermocatalytic durability. After 70 h of reaction, its r_{CO} and r_{H_2} values remain almost unchanged (Fig. 6B). The η value of $\text{Co}/\text{Co}-\text{Al}_2\text{O}_3$ is still as high as 23.6%. This result indicates that, compared with Co nanoparticles supported on Al_2O_3 nanosheets ($\text{Co}/\text{Al}_2\text{O}_3$), supporting Co nanoparticles on Co doped Al_2O_3 nanosheets ($\text{Co}/\text{Co}-\text{Al}_2\text{O}_3$) dramatically promotes photothermocatalytic durability in spite of the low photothermocatalytic activity of $\text{Co}-\text{Al}_2\text{O}_3$.

To reveal the origin of the dramatic improvement in durability, after the photothermocatalytic durability tests, the used samples of $\text{Co}/\text{Co}-\text{Al}_2\text{O}_3$ and $\text{Co}/\text{Al}_2\text{O}_3$ were characterized by TG-MS, XRD, and TEM. TG-MS shows that there are 63.14% and 39.7% weight losses for the used samples of $\text{Co}/\text{Co}-\text{Al}_2\text{O}_3$ and $\text{Co}/\text{Al}_2\text{O}_3$ due to the combustion of the deposited carbon

(Fig. S12, ESI[†]). Based on the weight loss, the carbon deposition rates (r_{C}) of $\text{Co}/\text{Co}-\text{Al}_2\text{O}_3$ and $\text{Co}/\text{Al}_2\text{O}_3$ are calculated to be 0.024 and 0.165 $\text{g}_{\text{C}} \text{g}_{\text{catalyst}}^{-1} \text{h}^{-1}$, respectively. The r_{C} value of $\text{Co}/\text{Co}-\text{Al}_2\text{O}_3$ being much less than that of $\text{Co}/\text{Al}_2\text{O}_3$ indicates that carbon deposition is dramatically inhibited by supporting Co nanoparticles on Co doped Al_2O_3 nanosheets. XRD analysis shows that the deposited carbon exists in the form of rhombohedral carbon (PDF 75-2078) in the used samples of $\text{Co}/\text{Co}-\text{Al}_2\text{O}_3$ and $\text{Co}/\text{Al}_2\text{O}_3$ (Fig. S13, ESI[†]). TEM shows that there are a lot of carbon nanofibers in the used samples of $\text{Co}/\text{Al}_2\text{O}_3$ (Fig. S14A, ESI[†]) and $\text{Co}/\text{Co}-\text{Al}_2\text{O}_3$ (Fig. S15A, ESI[†]). To reveal why the carbon deposition quickly deactivates $\text{Co}/\text{Al}_2\text{O}_3$, but does not cause $\text{Co}/\text{Co}-\text{Al}_2\text{O}_3$ to obviously lose photothermocatalytic activity, the used samples were characterized by HRTEM. As shown in Fig. S14B (ESI[†]), a lattice spacing of $\{111\}$ facets of carbon is observed around the Co nanoparticle for the used $\text{Co}/\text{Al}_2\text{O}_3$ sample, and the surface of the Co nanoparticle becomes obscure. This observation indicates that the surface of the Co nanoparticle is covered by a layer of amorphous carbon, which blocks the adsorption and subsequent reaction of CO_2 and CH_4 molecules. In striking contrast, although the lattice spacing of carbon is observed around the metallic Co nanoparticle for the used $\text{Co}/\text{Co}-\text{Al}_2\text{O}_3$ sample, a relatively clear lattice spacing of the metallic Co nanoparticle is still observed (Fig. S15B, ESI[†]). This observation indicates that carbon deposition on the surface of the Co nanoparticles in $\text{Co}/\text{Co}-\text{Al}_2\text{O}_3$ is inhibited, resulting in the excellent photothermocatalytic durability. This result further confirms that Co nanoparticles act as catalytically active sites for $\text{Co}/\text{Al}_2\text{O}_3$ and $\text{Co}/\text{Co}-\text{Al}_2\text{O}_3$.

2.4. Origin of the improved photothermocatalytic durability

To gain insight into the origin of the substantial improvement in photothermocatalytic durability of $\text{Co}/\text{Co}-\text{Al}_2\text{O}_3$, an isotope labeling experiment of photothermocatalytic $^{12}\text{C}^{18}\text{O}_2$ reduction by $^{12}\text{CH}_4$ on $\text{Co}/\text{Co}-\text{Al}_2\text{O}_3$ with focused UV-vis-IR irradiation was conducted (Experimental). With UV-vis-IR irradiation, accompanying the attenuation of C-H stretching peaks of $^{12}\text{CH}_4$ around 3016 cm^{-1} and C-O stretching peaks of $^{12}\text{C}^{18}\text{O}_2$ at 2324 and 2308 cm^{-1} , there are four peaks at 2169 , 2127 , 2116 , and 2081 cm^{-1} observed (Fig. 7A). The two peaks at 2169 and 2116 cm^{-1} are attributed to C-O stretching modes of $^{12}\text{C}^{16}\text{O}$, while the two peaks at 2127 and 2081 cm^{-1} are attributed to C-O stretching modes of $^{12}\text{C}^{18}\text{O}$.^{46,49} The formation of $^{12}\text{C}^{16}\text{O}$ indicates that O atoms from Co doped Al_2O_3 in $\text{Co}/\text{Co}-\text{Al}_2\text{O}_3$ participates in the oxidation of C^* species formed by both the complete dissociation of CH_4 and the disproportionation of the produced CO as side-reactions of carbon deposition. This is favorable for reducing the carbon deposition rate, thus improving the photothermocatalytic durability of $\text{Co}/\text{Co}-\text{Al}_2\text{O}_3$ compared to $\text{Co}/\text{Al}_2\text{O}_3$.

The participation of O atoms from Co doped Al_2O_3 in the oxidation of C^* species is further verified by Raman spectroscopy (Fig. 7B). The fresh $\text{Co}/\text{Co}-\text{Al}_2\text{O}_3$ sample has a Raman peak at around 689 cm^{-1} , which is attributed to the Co- ^{16}O stretching of Co doped Al_2O_3 ,⁵⁰ as $\gamma\text{-Al}_2\text{O}_3$ has no Raman peaks due to its very strong fluorescence background.⁵¹ The peak of the used $\text{Co}/\text{Co}-\text{Al}_2\text{O}_3$ sample shifts to 664 cm^{-1} . The obvious

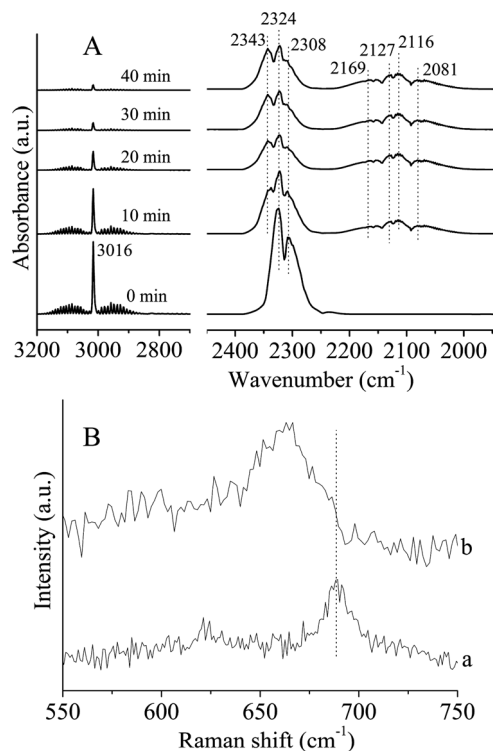


Fig. 7 Time course of FTIR spectra of the reactants and products for $^{12}\text{C}^{18}\text{O}_2$ reduction by $^{12}\text{C}^1\text{H}_4$ on $\text{Co}/\text{Co}-\text{Al}_2\text{O}_3$ with focused UV-vis-IR irradiation (A). Raman spectra (B) of the fresh $\text{Co}/\text{Co}-\text{Al}_2\text{O}_3$ sample (a) and the used $\text{Co}/\text{Co}-\text{Al}_2\text{O}_3$ sample after testing photothermocatalytic $^{12}\text{C}^{18}\text{O}_2$ reduction with $^{12}\text{C}^1\text{H}_4$ (b). Note: in Fig. 7A, a shoulder peak at 2343 cm^{-1} is attributed to the C–O stretching of $^{12}\text{C}^{18}\text{O}^{16}\text{O}$,⁴⁶ indicating that O atoms from Co doped Al_2O_3 in $\text{Co}/\text{Co}-\text{Al}_2\text{O}_3$ also participate in the oxidation of C^{18}O .

isotope shift clearly indicates that $\text{Co}-^{16}\text{O}$ bonds of $\text{Co}/\text{Co}-\text{Al}_2\text{O}_3$ transform to $\text{Co}-^{18}\text{O}$ bonds due to the following reactions: the formed $^{12}\text{C}^*$ species are oxidized to $^{12}\text{C}^{16}\text{O}$ by ^{16}O atoms of $\text{Co}-\text{Al}_2\text{O}_3$ in $\text{Co}/\text{Co}-\text{Al}_2\text{O}_3$ (Fig. 7A). $^{12}\text{C}^{18}\text{O}_2$ molecules adsorbed on the resultant ^{16}O vacancies dissociate to $^{12}\text{C}^{18}\text{O}$ and $^{18}\text{O}^*$, resulting in refilling of ^{16}O vacancies in $\text{Co}-\text{Al}_2\text{O}_3$ by $^{18}\text{O}^*$.

2.5. Roles of light

2.5.1. Heating: light-driven thermocatalysis. In order to unveil why $\text{Co}/\text{Co}-\text{Al}_2\text{O}_3$ has high photothermocatalytic activity, the absorption spectra of the samples were recorded (Fig. 8A). $\text{Co}-\text{Al}_2\text{O}_3$ has two strong absorption bands in the regions of 470–700 nm and 960–1850 nm. $\text{Co}/\text{Co}-\text{Al}_2\text{O}_3$ has strong absorption over the whole solar spectrum region, which is attributed to the strong surface plasmon absorption of Co nanoparticles overlapping with the absorption of $\text{Co}-\text{Al}_2\text{O}_3$.

To confirm whether the strong absorption of $\text{Co}/\text{Co}-\text{Al}_2\text{O}_3$ causes photocatalytic activity, photocatalytic CO_2 reduction by CH_4 on $\text{Co}/\text{Co}-\text{Al}_2\text{O}_3$ with UV-vis-IR irradiation was performed at near room temperature. CO and H_2 are not detected by GC (Fig. S16, ESI†). This result suggests that the high photothermocatalytic activity of $\text{Co}/\text{Co}-\text{Al}_2\text{O}_3$ (Fig. 4) can be ascribed to light-driven thermocatalysis rather than photocatalysis.

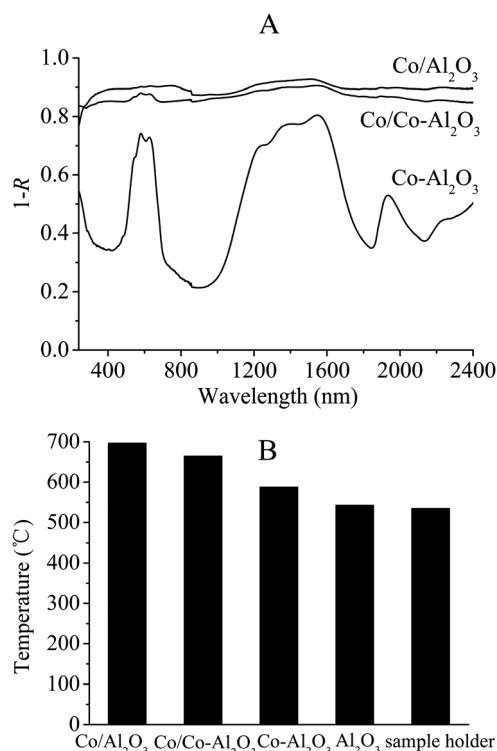


Fig. 8 Diffusive reflectance absorption spectra of Al_2O_3 , $\text{Co}-\text{Al}_2\text{O}_3$, $\text{Co}/\text{Al}_2\text{O}_3$, and $\text{Co}/\text{Co}-\text{Al}_2\text{O}_3$ (A): R is reflectance (%). The T_{eq} values of Al_2O_3 , $\text{Co}-\text{Al}_2\text{O}_3$, $\text{Co}/\text{Al}_2\text{O}_3$, $\text{Co}/\text{Co}-\text{Al}_2\text{O}_3$, and the sample holder with focused UV-vis-IR irradiation (B).

Upon the focused irradiation, the surface temperature of $\text{Co}/\text{Co}-\text{Al}_2\text{O}_3$ is quickly raised to an equilibrium temperature (T_{eq}). When the T_{eq} value exceeds the light-off temperature ($T_{\text{light-off}}$: the temperature at which the thermocatalytic reaction starts to proceed) of thermocatalytic CO_2 reduction by CH_4 on $\text{Co}/\text{Co}-\text{Al}_2\text{O}_3$, the thermocatalytic reaction is triggered.

The T_{eq} values of the samples with focused irradiation were measured. The T_{eq} values of $\text{Co}-\text{Al}_2\text{O}_3$, $\text{Co}/\text{Co}-\text{Al}_2\text{O}_3$, and $\text{Co}/\text{Al}_2\text{O}_3$ with focused UV-vis-IR irradiation are 588, 665, and 697 °C, respectively (Fig. 8B). The T_{eq} values of $\text{Co}/\text{Co}-\text{Al}_2\text{O}_3$ with focused vis-IR irradiation of $\lambda > 420$, 560, and 690 nm are 612, 554, and 497 °C, respectively (Fig. S17, ESI†). The high T_{eq} values are ascribed to the IR heating effect of the focused irradiation as well as photothermal conversion owing to the strong absorption by the samples (Fig. 8A). The IR heating effect is confirmed by the high T_{eq} value of the sample holder (535 °C).

Thermocatalytic CO_2 reduction by CH_4 on the samples in the dark was evaluated (Fig. 9). The thermocatalytic activity of $\text{Co}-\text{Al}_2\text{O}_3$ is very low. $\text{Co}/\text{Al}_2\text{O}_3$ shows higher thermocatalytic activity than $\text{Co}-\text{Al}_2\text{O}_3$. Compared to $\text{Co}/\text{Al}_2\text{O}_3$, the thermocatalytic activity of $\text{Co}/\text{Co}-\text{Al}_2\text{O}_3$ is significantly enhanced. This enhancement indicates the presence of a synergetic effect between Co nanoparticles and $\text{Co}-\text{Al}_2\text{O}_3$ due to the fact that O atoms from $\text{Co}-\text{Al}_2\text{O}_3$ participate in the CO_2 reduction with CH_4 (as discussed in Section 2.4). The $T_{\text{light-off}}$ values of $\text{Co}-\text{Al}_2\text{O}_3$, $\text{Co}/\text{Al}_2\text{O}_3$, and $\text{Co}/\text{Co}-\text{Al}_2\text{O}_3$ are about 651, 647, and 490 °C, respectively (Fig. 9A and B). They are less than their

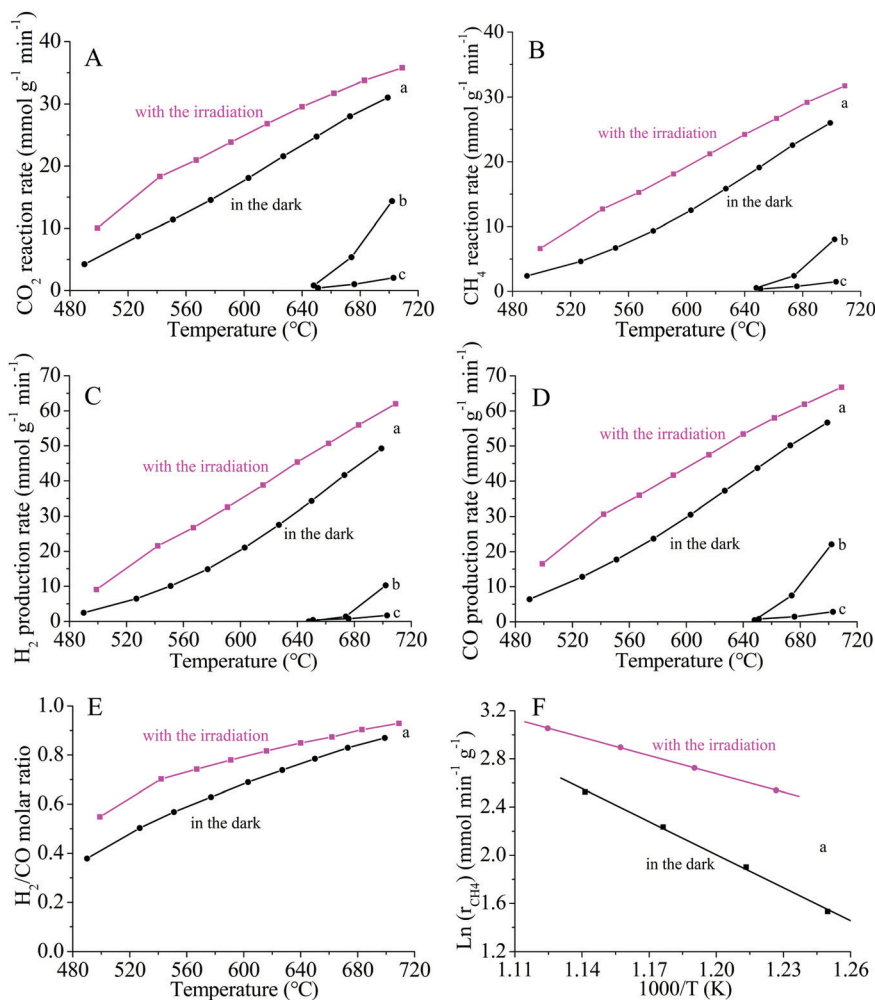


Fig. 9 CO₂ reaction rate (A), CH₄ reaction rate (B), H₂ production rate (C), CO production rate (D), and H₂/CO molar ratio (E) vs. T , and $\ln(r_{\text{CH}_4})$ vs. $1/T$ (F) for CO₂ reduction with CH₄ on Co/Co–Al₂O₃ in the dark and under focused UV-vis-IR irradiation (a), Co/Al₂O₃ in the dark (b), and Co–Al₂O₃ in the dark (c). Note: the thermocatalytic data of Co/Al₂O₃ in A–D are the average data in the initial 20 min as Co/Al₂O₃ experienced swift deactivation (see Fig. 6A).

corresponding T_{eq} values (Fig. 8B). Therefore, light-driven thermocatalytic CO₂ reduction by CH₄ is able to proceed.

2.5.2. Photoactivation. Is the high photothermocatalytic activity of Co/Co–Al₂O₃ merely accredited to the light-driven thermocatalysis? To address this issue, CO₂ reduction by CH₄ on Co/Co–Al₂O₃ at the same temperature was conducted in the dark and with focused irradiation. At the same temperature greater than 490 °C, in comparison with the corresponding values obtained in the dark, the focused UV-vis-IR irradiation substantially raises the values of r_{CO_2} , r_{CH_4} , r_{H_2} , r_{CO} , and the H₂/CO molar ratio (Fig. 9A–E). Similar enhancements in the catalytic activity of Co/Co–Al₂O₃ with focused vis-IR irradiation of $\lambda > 420$ and 560 nm are observed (Fig. S18, ESI†). As Co/Co–Al₂O₃ has no photocatalytic activity (Fig. S16, ESI†), the result suggests that the substantial catalytic enhancement is caused by a new photoactivation effect. The enhancement in the H₂/CO molar ratio is attributed to the fact that the catalytic enhancement for the CO₂ reduction by CH₄ by focused vis-IR irradiation (Fig. 9C and D) is more pronounced than that for CO₂ reduction by H₂ as the aforementioned side-reaction (Fig. S19, ESI†).

Graphs of $\ln(r_{\text{CH}_4})$ vs. $1/T$ are plotted on the basis of the r_{CH_4} values of Co/Co–Al₂O₃ (Fig. 9B). A good linear relationship between $\ln(r_{\text{CH}_4})$ and $1/T$ is observed (Fig. 9E). In accordance with the Arrhenius equation ($k = Ae^{-E_{\text{a,app}}/RT}$), the apparent activation energy ($E_{\text{a,app}}$) value of Co/Co–Al₂O₃ with focused UV-vis-IR irradiation is calculated to be 42.0 kJ mol^{−1}. This is less than that in the dark (69.8 kJ mol^{−1}). This means that the focused UV-vis-IR irradiation substantially reduces the activation energy, thus considerably improving the catalytic activity.

CO₂ reduction by CH₄ involves a number of elementary steps, including the decomposition of CO₂ to CO* and O*, the step-by-step decompositions of CH₄ to CH_{*x*}* ($x = 0-3$), the oxidation of CH_{*x*} by O*, and so on.^{45,52} Among these steps, the oxidations of C* and CH* are the rate-determining steps due to their higher activation energies.^{45,52} To gain deep insight into the photoactivation, temperature-programmed reactions of CO₂ decomposition (CO₂-TPD), CH₄ decomposition (CH₄-TPD), and oxidation of pre-deposited CH_{*x*}* species by CO₂ (CH_{*x*}*-TPO) on Co/Co–Al₂O₃ were conducted in the dark and under irradiation (see Experimental, ESI†). CO₂-TPD shows that UV-vis-IR irradiation

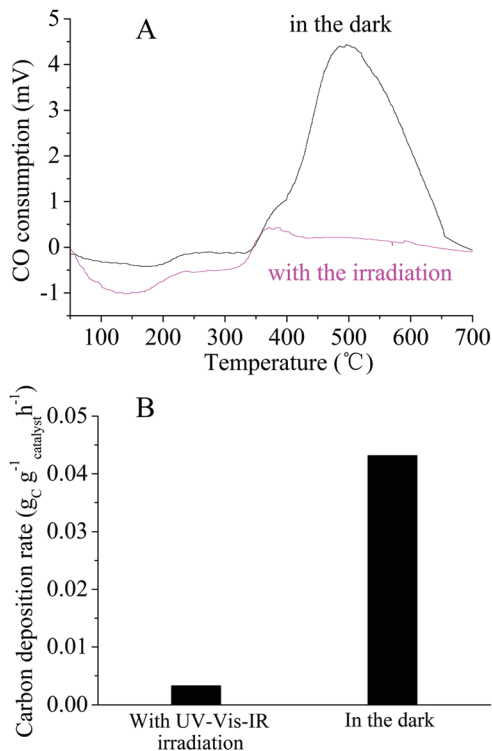


Fig. 10 The CO-TPD profiles of Co/Co–Al₂O₃ (A) and corresponding carbon deposition rates (B) in the dark and with focused UV-vis-IR irradiation.

does not obviously affect CO₂ decomposition (Fig. S20, ESI[†]). CH₄-TPD shows that UV-vis-IR irradiation causes a slight shift in the CH₄ consumption peak to 653 °C compared to that in the dark (662 °C, Fig. S21, ESI[†]). This indicates that UV-vis-IR irradiation slightly promotes CH₄ decomposition. Interestingly, compared to the CH_x-TPO profile in the dark, the UV-vis-IR irradiation significantly promotes the oxidation of pre-deposited CH_x* species as a rate-determining step (Fig. S22, ESI[†]). Similar promotion for the oxidation of pre-deposited CH_x* species on Co/Co–Al₂O₃ with vis-IR irradiation of $\lambda > 420$ and 560 nm is observed (Fig. S22, ESI[†]).

To unveil whether the photoactivation affects carbon deposition, temperature-programmed CO disproportionation (a major side-reaction of carbon deposition) on Co/Co–Al₂O₃ was conducted in the dark and under irradiation (see Experimental, ESI[†]). Compared to the profile in the dark, the CO consumption peak around 497 °C due to CO disproportionation is significantly reduced upon UV-vis-IR irradiation (Fig. 10A). The carbon deposition rate (r_C) with UV-vis-IR irradiation is calculated to be $3.3 \times 10^{-3} \text{ g}_C \text{g}_{\text{catalyst}}^{-1} \text{ h}^{-1}$, which is 13 times lower than that in the dark (Fig. 10B). Similar inhibition of CO disproportionation on Co/Co–Al₂O₃ with vis-IR irradiation of $\lambda > 420$ and 560 nm is observed (Fig. S23, ESI[†]). This result indicates that the photoactivation also significantly reduces the carbon deposition rate, thus improving photothermocatalytic durability.

3. Conclusions

In conclusion, a unique nanocomposite of Co nanoparticles supported on Co doped Al₂O₃ nanosheets (Co/Co–Al₂O₃) was

synthesized. With focused UV-vis-IR irradiation, Co/Co–Al₂O₃ shows high light-to-fuel efficiency and production rates of CO and H₂ for photothermocatalytic CO₂ reduction by CH₄. Compared to the reference Co/Al₂O₃ catalyst, the formation of the unique Co/Co–Al₂O₃ nanocomposite significantly promotes catalyst durability. The improved durability is ascribed to the fact that O atoms of Co–Al₂O₃ at the interface of Co nanoparticles and Co doped Al₂O₃ accelerate the oxidation of C* species formed by both CH₄ dissociation and CO disproportionation as side reactions of carbon deposition. The high photothermocatalytic activity is ascribed to effective light-driven thermocatalysis substantially boosted by new photoactivation: the focused UV-vis-IR irradiation substantially reduces the activation energy, thus considerably improving the catalytic activity. The new photoactivation also significantly inhibits the side reaction of CO disproportionation, thus promoting catalyst durability. This work actualizes extremely effective CO₂ reduction to fuels with high light-to-fuel efficiency and excellent catalyst durability, which is very promising for tackling the issues of solar energy storage and global warming induced by CO₂.

Conflicts of interest

There are no conflicts to declare.

Acknowledgements

This work was supported by the National Natural Science Foundation of China (21673168, 21473127).

References

- 1 G. Zhang, G. Liu, L. Z. Wang and J. T. S. Irvine, *Chem. Soc. Rev.*, 2016, **45**, 5951–5984.
- 2 S. J. A. Moniz, S. A. Shevlin, D. J. Martin, Z. X. Guo and J. W. Tang, *Energy Environ. Sci.*, 2015, **8**, 731–759.
- 3 Y. Wang, H. Suzuki, J. Xie, O. Tomita, D. J. Martin, M. Higashi, D. Kong, R. Abe and J. W. Tang, *Chem. Rev.*, 2018, **118**, 5201–5241.
- 4 J. Liu, Y. Liu, N. Y. Liu, Y. Z. Han, X. Zhang, H. Huang, Y. Lifshitz, S. T. Lee, J. Zhong and Z. H. Kang, *Science*, 2015, **347**, 970–974.
- 5 L. Yu, H. Q. Zhou, J. Y. Sun, F. Qin, F. Yu, J. M. Bao, Y. Yu, S. Chen and Z. F. Ren, *Energy Environ. Sci.*, 2017, **10**, 1820–1827.
- 6 Q. Zhang, Z. Li, S. Y. Wang, R. G. Li, X. W. Zhang, Z. X. Liang, H. X. Han, S. J. Liao and C. Li, *ACS Catal.*, 2016, **6**, 2182–2191.
- 7 Q. Yuan, D. Liu, N. Zhang, W. Ye, H. Ju, L. Shi, R. Long, J. Zhu and Y. Xiong, *Angew. Chem., Int. Ed.*, 2017, **56**, 4206.
- 8 B. Mei, K. Han and G. Mul, *ACS Catal.*, 2018, **8**, 9154–9164.
- 9 C. W. Dong, S. Y. Lu, S. Y. Yao, R. Ge, Z. D. Wang, Z. Wang, P. F. An, Y. Liu, B. Yang and H. Zhang, *ACS Catal.*, 2018, **8**, 8649–8658.
- 10 P. Li, X. Chen, H. He, X. Zhou, Y. Zhou and Z. Zou, *Adv. Mater.*, 2018, **30**, 1703119.

- 11 I. Ivanova, T. A. Kandiell, Y. J. Cho, W. Y. Choi and D. Bahnemann, *ACS Catal.*, 2018, **8**, 2313–2325.
- 12 M. Xiao, B. Luo, M. Lyu, S. Wang and L. Wang, *Adv. Energy Mater.*, 2018, **8**, 1701605.
- 13 Z. F. Jiang, H. L. Sun, T. Q. Wang, B. Wang, W. Wei, H. M. Li, S. Q. Yuan, T. C. An, H. J. Zhao, J. G. Yu and P. K. Wong, *Energy Environ. Sci.*, 2018, **11**, 2382–2389.
- 14 X. C. Jiao, X. D. Li, X. Y. Jin, Y. F. Sun, J. Q. Xu, L. Liang, H. X. Ju, J. F. Zhu, Y. Pan, W. S. Yan, Y. Lin and Y. Xie, *J. Am. Chem. Soc.*, 2017, **139**, 18044–18051.
- 15 L. Liang, F. C. Lei, S. Gao, Y. F. Sun, X. C. Jiao, J. Wu, S. Qamar and Y. Xie, *Angew. Chem., Int. Ed.*, 2015, **54**, 13971–13974.
- 16 S. Y. Zhu, S. J. Liang, J. H. Bi, M. H. Liu, L. M. Zhou, L. Wu and X. X. Wang, *Green Chem.*, 2016, **18**, 1355–1363.
- 17 S. Y. Zhu, S. J. Liang, Y. Wang, X. Y. Zhang, F. Y. Li, H. X. Lin, Z. Z. Zhang and X. X. Wang, *Appl. Catal., B*, 2016, **187**, 11–18.
- 18 L. Yuan, K. Q. Lu, F. Zhang, X. Z. Fu and Y. J. Xu, *Appl. Catal., B*, 2018, **237**, 424–431.
- 19 F. Raziq, Y. Qu, M. Humayun, A. Zada, H. T. Yu and L. Q. Jing, *Appl. Catal., B*, 2017, **201**, 486–494.
- 20 J. S. Wang, C. L. Qin, H. J. Wang, M. N. Chu, A. Zada, X. L. Zhang, J. D. Li, F. Raziq, Y. Qu and L. Q. Jing, *Appl. Catal., B*, 2018, **221**, 459–466.
- 21 Y. F. Zhao, G. B. Chen, T. Bian, C. Zhou, G. I. N. Waterhouse, L. Z. Wu, C. H. Tung, L. J. Smith, D. O'Hare and T. R. Zhang, *Adv. Mater.*, 2015, **27**, 7824–7831.
- 22 S. W. Cao, B. J. Shen, T. Tong, J. W. Fu and J. G. Yu, *Adv. Funct. Mater.*, 2018, **28**, 1800136.
- 23 Q. G. Zhai, S. J. Xie, W. Q. Fan, Q. H. Zhang, Y. Wang, W. P. Deng and Y. Wang, *Angew. Chem.*, 2013, **125**, 5888–5891.
- 24 L. Lu, B. Wang, S. M. Wang, Z. Shi, S. C. Yan and Z. G. Zou, *Adv. Funct. Mater.*, 2017, **27**, 1702447.
- 25 G. Yang, D. M. Chen, H. Ding, J. J. Feng, J. Z. Zhang, Y. F. Zhu, S. Hamid and D. W. Bahnemann, *Appl. Catal., B*, 2017, **219**, 611–618.
- 26 U. Kang, S. K. Choi, D. J. Ham, S. M. Ji, W. Y. Choi, D. S. Han, A. Abdel-Wahab and H. Park, *Energy Environ. Sci.*, 2015, **8**, 2638–2643.
- 27 M. Zhou, S. B. Wang, P. J. Yang, C. J. Huang and X. C. Wang, *ACS Catal.*, 2018, **8**, 4928–4936.
- 28 B. Han, X. W. Ou, Z. Q. Deng, Y. Song, C. Tian, H. Deng, Y. J. Xu and Z. Lin, *Angew. Chem., Int. Ed.*, 2018, **57**, 16811–16815.
- 29 S. B. Wang, B. Y. Guan and X. W. Lou, *Energy Environ. Sci.*, 2018, **11**, 306–310.
- 30 S. B. Wang, B. Y. Guan and X. W. Lou, *J. Am. Chem. Soc.*, 2018, **140**, 5037–5040.
- 31 X. Q. An, K. F. Li and J. W. Tang, *ChemSusChem*, 2014, **7**, 1086–1093.
- 32 X. J. Wang, X. L. Zhao, D. Q. Zhang, G. S. Li and H. X. Li, *Appl. Catal., B*, 2018, **228**, 47–53.
- 33 W. N. Wang, W. J. An, B. Ramalingam, S. Mukherjee, D. M. Niedzwiedzki, S. Gangopadhyay and P. Biswas, *J. Am. Chem. Soc.*, 2012, **134**, 11276–11281.
- 34 L. Yuliati and H. Yoshida, *Chem. Soc. Rev.*, 2008, **37**, 1592–1602.
- 35 G. Mahmodi, S. Sharifnia, M. Madani and V. Vatanpour, *Sol. Energy*, 2013, **97**, 186–194.
- 36 J. W. Tang, J. R. Durrant and D. R. Klug, *J. Am. Chem. Soc.*, 2008, **130**, 13885–13891.
- 37 M. Kong, Y. Z. Li, X. Chen, T. T. Tian, P. F. Fang, F. Zheng and X. J. Zhao, *J. Am. Chem. Soc.*, 2011, **133**, 16414–16417.
- 38 S. X. Ouyang and J. H. Ye, *J. Am. Chem. Soc.*, 2011, **133**, 7757–7763.
- 39 M. Y. Mao, Y. Z. Li, J. T. Hou, M. Zeng and X. J. Zhao, *Appl. Catal., B*, 2015, **174**, 496–503.
- 40 B. A. Pinaud, J. D. Benck, L. C. Seitz, A. J. Forman, Z. Chen, T. G. Deutsch, B. D. James, K. N. Baum, G. N. Baum, S. Ardo, H. Wang, E. Miller and T. F. Jaramillo, *Energy Environ. Sci.*, 2013, **6**, 1983–2002.
- 41 B. Han, W. Wei, L. Chang, P. F. Cheng and Y. H. Hu, *ACS Catal.*, 2016, **6**, 494–497.
- 42 H. M. Liu, X. G. Meng, T. D. Dao, H. B. Zhang, P. Li, K. Chang, T. Wang, M. Li, T. Nagao and J. H. Ye, *Angew. Chem., Int. Ed.*, 2015, **54**, 11545–11549.
- 43 H. M. Liu, T. D. Dao, L. Q. Liu, X. G. Meng, T. Nagao and J. H. Ye, *Appl. Catal., B*, 2017, **209**, 183–189.
- 44 Y. Sun, T. Ritchie, S. S. Hla, S. McEvoy, W. Stein and J. H. Edwards, *J. Nat. Gas Chem.*, 2011, **20**, 568–576.
- 45 H. Huang, M. Y. Mao, Q. Zhang, Y. Z. Li, J. L. Bai, Y. Yang, M. Zeng and X. J. Zhao, *Adv. Energy Mater.*, 2018, 1702472.
- 46 M. Y. Mao, Q. Zhang, Y. Yang, Y. Z. Li, H. Huang, Z. K. Jiang, Q. Q. Hu and X. J. Zhao, *Green Chem.*, 2018, **20**, 2857–2869.
- 47 Q. Zhang, M. Y. Mao, Y. Z. Li, Y. Yang, H. Huang, Z. K. Jiang, Q. Q. Hu, S. W. Wu and X. J. Zhao, *Appl. Catal., B*, 2018, **239**, 555–564.
- 48 D. Marxer, P. Furler, M. Takacs and A. Steinfeld, *Energy Environ. Sci.*, 2017, **10**, 1142–1149.
- 49 B. S. Shete, V. S. Kamble, N. M. Gupta and V. B. Kartha, *Phys. Chem. Chem. Phys.*, 1999, **1**, 191–198.
- 50 B. Jongsomjit, J. Panpranot and J. G. Goodwin, *J. Catal.*, 2001, **204**, 98–109.
- 51 A. Aminzadeh and H. Sarikhani-fard, *Spectrochim. Acta, Part A*, 1999, **55**, 1421–1425.
- 52 Y. A. Zhu, D. Chen, X. G. Zhou and W. K. Yuan, *Catal. Today*, 2009, **148**, 260–267.